Selected Paper

Theoretical Studies on Electronic Structures and Chemical Indices of the Active Site of Oxygenated and Deoxygenated Hemerythrin

Yu Takano,*,† Hiroshi Isobe, and Kizashi Yamaguchi

Department of Chemistry, Graduate School of Science, Osaka University, Toyonaka, Osaka 560-0043

Received May 14, 2007; E-mail: ytakano@protein.osaka-u.ac.jp

Hemerythrin (Hr) is an oxygen-transport protein that includes a binuclear iron active site, which is found in marine invertebrates. We investigated the origin of the magnetic couplings, the nature of the chemical bond, and the mechanism of the dioxygen binding of Hr using an appropriate theoretical method and realistic models. First, we selected the appropriate functional of DFT; spin-polarized Becke's half and half LYP (UB2LYP) showed reasonably good agreement with the experimental values. Secondly, in order to elucidate the origin of the magnetic couplings and understand the nature of the chemical bond, we estimated a range of chemical indices using natural orbitals obtained at the UB2LYP level. The results indicate that the origin of the antiferromagnetic coupling for Hr is the σ- and π-type orbital interactions via weak Fe–μO conjugation (σ- and π-type superexchange interactions) and that the difference in the strength of the dσ–pσ and dπ–pπ interactions of the diiron core in the active site of Hr is responsible for the difference in the magnetic coupling constants between oxygenated and deoxygenated Hr. Finally, using the Mulliken charge-transfer theory, we analyzed the ionization potentials of molecular oxygen and Hr. We concluded that the dioxygen binding in Hr would proceed via a two-step electron-transfer mechanism.

Diiron complexes with μ-O and/or μ-OH bridges, which function as O_2 transporters and oxygen activators for oxygenation, are found in the active core of a number of proteins. Over the past few decades, the complexes have received great interest both experimentally and theoretically. These cores are found in hemerythrin (Hr),[1] methane monooxygenase (MMO), ribonucleotide reductase (RNR), and Δ^9-stearoyl-acyl carrier protein desaturase. Figure 1 illustrates the main skeletons of Hr (**A**), MMO (**B**), and RNR (**C**) in the oxygenated forms. These skeletons are similar to each other. In addition, the iron ions in these systems are locally high-spin (HS), and they are exchange-coupled antiferromagnetically. So far, enormous numbers of diiron complexes have been synthesized as models of active sites of these enzymes to not only understand the biological functions but also to develop new functional molecules inspired from biology.[2] Since it is helpful to investigate the electronic structures of the diiron active sites in the metalloproteins in order to elucidate the biological mechanism and to design new diiron complexes, many theoretical calculations have also been performed on these model complexes.

Hr is one of the three major oxygen-transport proteins,[1] and it is found in several marine invertebrates, including *Sipunculida*, *Priapulida*, and *Brachiopoda*. Two physiologically relevant forms of Hr are deoxygenated (deoxyHr) and oxygenated (oxyHr) states. Crystallographic[3] and spectroscopic[4,5] studies on deoxyHr have shown that the active site consists of two Fe^{II} ions bridged by two carboxylate and one μ-OH groups. The coordination spheres of the two iron ions are completed by five histidine-*N* ligands, three binding to the six-coordinate (Fe1) and two to the five-coordinate (Fe2) metal centers. In deoxyHr, the magnetic coupling constant (J_{ab}) has been experimentally determined to be $-14\,cm^{-1}$.[6] Upon the reaction of deoxyHr with molecular oxygen, two electrons from the Fe^{II}–Fe^{II} center and a proton from the bridging μ-OH group are transferred to the O_2 bound to Fe2, yielding a μ-O-bridged diferric site possessing a terminal hydroperoxide (oxyHr). The presence of the μ-O bridge at the active site in oxyHr gives rise to stronger antiferromagnetic coupling between the two Fe^{III} ions: $J_{ab} = -77\,cm^{-1}$.

Synthetic modeling approaches[7] have greatly increased our understanding of the electronic structure of the binuclear iron site in Hr. Armstrong and Lippard have synthesized [Fe_2-(μ-O)(μ-CH_3COO)$_2$(HB(3,5-*i*Pr_2-Pz)$_3$)$_2$] (HB(3,5-*i*Pr_2-Pz)$_3$ = hydrotris(3,5-diisopropylpyrazolyl)borate)[7a] (Fig. 1A(a)), which is a model of azidomet Hr. The coupling constant between the two ferric centers has been determined to be -121 cm^{-1}. For deoxyHr, [Fe(μ-OH)(μ-CH_3COO)$_2$(Me_3TACN)$_2$] (Me_3TACN = 1,4,7-trimethyl-1,4,7-triazacyclononane)[7b] has been synthesized (Fig. 1A(b)). The magnetic coupling constant has been found to be $-13\,cm^{-1}$ by using SQUID magnetic susceptibility measurements.

Recently, Brunold and Solomon have investigated the magnetic couplings of both deoxy and oxyHr by using SQUID susceptibility experiment and have evaluated the J_{ab} values for Hr models, [(NH_3)$_3$Fe(μ-OH)(μ-HCOO)$_2$Fe(NH_3)$_2$] and [(NH_3)$_3$Fe(μ-O)(μ-HCOO)$_2$Fe(OOH)(NH_3)$_2$], by using density functional (DFT) calculations.[6] They have employed the local density approximation of Vosko, Wilk, and Nusair[8] and the nonlocal gradient corrections of Becke[9] and Perdew.[10] However, the estimated $|J_{ab}|$ value for the simple model of oxyHr is much larger than that determined experimentally,[4] and that of deoxyHr is inconsistent with the experimental value even qualitatively.[6] Rodriguez and McCusker have

† Present address: Institute for Protein Research, Osaka University, Suita, Osaka 565-0871

Published on the web January 10, 2008; doi:10.1246/bcsj.81.91

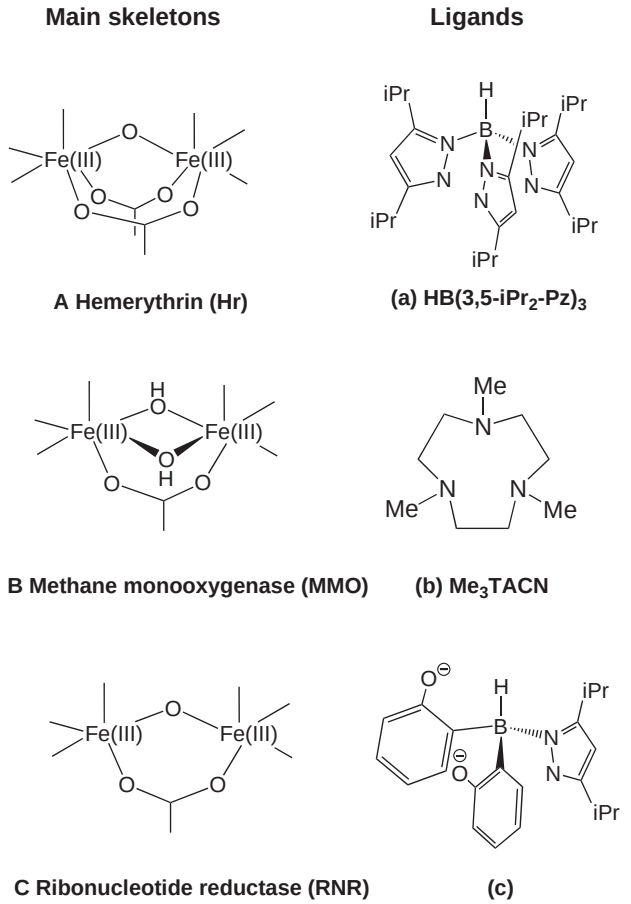

Fig. 1. Main skeletons of hemerythrin (Hr) (**A**), methane monooxygenase (MMO) (**B**), and ribonucleotide reductase (RNR) (**C**) and coordination ligands utilized for the models of Hr; $HBpz_3$ = hydrotris(3,5-diisopropylpyrazolyl)-borate (**a**), Me_3TACN = 1,4,7-trimethyl-1,4,7-triazacyclononane) (**b**), and a proposed ligand for oxygen activation (**c**).

examined the electronic structure and magnetic properties of two structurally characterized diferric model complexes, $[Fe_2(\mu\text{-}O)(\mu\text{-}CH_3COO)_2(HBpz_3)_2]$ and $[Fe_2(\mu\text{-}OH)(\mu\text{-}CH_3COO)_2(HBpz_3)_2]^+$ ($HBPz_3$ = hydrotrispyrazolylborate).[11] DFT calculations using a combination of Becke gradient-corrected exchange and Perdew–Wang nonlocal correlation (UBPW91)[9,10,12] have shown that the two complexes are strongly ($-76.35\,cm^{-1}$) and weakly ($-11.65\,cm^{-1}$) antiferromagnetically coupled in agreement with experiment. However, geometry optimizations at the high-spin states have only been reported. Wirstam, Lippard, and Friesner have determined the different energetic components involved in the reversible binding of O_2 to Hr using a combination of DFT methods and a mixed quantum mechanical/molecular mechanical (QM/MM) method.[13] They have reported that the major contributions from the protein environment stabilizing dioxygen binding are the van der Waals interaction between the bound dioxygen and the protein atoms, and an increase in the hydrogen bonding energy of an imidazole group, ligated to one of the iron atoms, and a neighboring carboxylate side chain in the second coordination sphere. Shoji et al. have also investigated the electronic structures for the Hr model compounds $[Fe_2(\mu\text{-}O)(\mu\text{-}CH_3COO)_2(HBpz_3)_2]$, $[Fe_2(\mu\text{-}OH)(\mu\text{-}CH_3COO)_2(HBpz_3)_2]^+$, $[Fe_2(\mu\text{-}O)(\mu\text{-}CH_3COO)_2(Me_3TACN)_2]^+$, and $[Fe_2(\mu\text{-}OH)(\mu\text{-}CH_3COO)_2(Me_3TACN)_2]^{2+}$ from the viewpoint of the magnetic interactions and chemical indices. The magnetic interactions calculated by using hybrid DFT methods are wholly consistent with the available experiment data.[14]

Previously, we have developed a computational scheme to calculate J_{ab} values based on broken-symmetry (BS) molecular orbital methods, such as unrestricted Hartree–Fock (UHF) method in combination of approximate spin projection (AP) procedure.[15] Many BS calculations have been carried out to elucidate exchange couplings in binuclear transition-metal complexes.

Recently, we have also performed UHF and spin-polarized DFT (UDFT) calculations (spin-polarized Becke's half and half LYP (UB2LYP),[16] UB3LYP,[17] and UBLYP[9,18]) on Cu^{II}–Cu^{II} complexes (**Hc**), which are models of oxyhemocyanin (oxyHc).[19] In the models, each Cu ion is coordinated by three methylimidazole or three ammonium (NH_3) ligands. We have examined the magnetic couplings for **Hc** with dioxygen (**Hc-O_2**) and dioxygen binding process, and we have concluded that the orbital interactions via the binding dioxygen, namely, superexchange (SE) interaction, cause strong antiferromagnetic coupling between the two copper ions of **Hc-O_2**. UB2LYP method has been found to be effective for strongly correlated electron systems, such as **Hc-O_2**. A realistic model using methylimidazole is required to form a stable complex.

Since magnetic coupling is sensitive to the electronic structure, such as chemical bonds, and several enzymes include transition-metal clusters in their active sites, it is important to employ realistic models for the active site and appropriate theoretical methods, which can evaluate the magnetic couplings, in order to examine the electronic structures of the active site of metalloproteins. In this study, the origin of the magnetic couplings, the nature of the chemical bond, and the mechanism of the dioxygen binding of the active site of Hr were examined with an appropriate theoretical method and realistic models. Our study consisted of three steps as follows. (i) first of all, we estimated J_{ab} values for a diferric complex **1** as a model of oxyHr and a diferrous complex **2** as a model of deoxyHr by using UHF, spin-polarized pure DFT (UBLYP), and hybrid DFT (UB2LYP, UB3LYP, and UB3LYP*[20]) methods. Comparing J_{ab} values, we found that UB2LYP can be regarded as a reliable method to investigate the magnetic couplings for oxy and deoxyHr. (ii) Next, on the basis of the best DFT functional, B2LYP, we examined the electronic structures of **1** and **2** from the viewpoint of the shape and symmetry of the natural orbitals (NOs) and chemical indices. The indices enabled us to obtain information about the nature of the chemical bonds of the active site of Hr, and they showed that the oxyHr has weak chemical bonds in the active core, which lead to the reversible dioxygen trapping. (iii) Finally, ionization potentials of electron-donating orbitals were calculated in order to evaluate the charge-transfer interactions between molecular oxygen and Hr in dioxygen binding. Mulliken charge-transfer (CT) theory is a useful guide for understanding the intermolecular interaction between triplet molecular oxygen and electron donor.[19b,21] CT theory was applied to the dioxy-

gen association in deoxyHr. UB2LYP results were consistent with a stepwise mechanism for oxygen trapping of deoxyHr.

Theoretical Background[22]

Quantum Mechanical Calculations of J_{ab}. We considered the magnetic couplings between Fe ions of **1** and **2**. Model **1** includes two high-spin Fe^{III} ions, bridging μ-O and acetate groups, whereas two high-spin Fe^{II} ions interact with each other via μ-OH and acetate ligands in **2**. The magnetic couplings for **1** and **2** can be regarded as the spin interactions between the two localized spin sites, which consist of Fe^{III} ions ($S = 5/2$) for **1** and Fe^{II} ions ($S = 2$) for **2** via the bridging ligands. In this study, the J_{ab} values were estimated by using several computational methods, Eqs. 1a–1c:

$$J_{ab}^{(1)} = \frac{^{LS}E_X - {}^{HS}E_X}{S_{max}^2}, \tag{1a}$$

$$J_{ab}^{(2)} = \frac{^{LS}E_X - {}^{HS}E_X}{S_{max}(S_{max}+1)}, \tag{1b}$$

$$J_{ab}^{(3)} = \frac{^{LS}E_X - {}^{HS}E_X}{^{HS}\langle S^2\rangle_X - {}^{LS}\langle S^2\rangle_X}, \tag{1c}$$

where $^{Y}E_X$ and $^{Y}\langle S^2\rangle_X$ denote the total energy and total angular momentum of the spin state Y (Y = LS (lowest spin state) and HS (highest spin state)) by using method X (X = UHF and UDFT), respectively, and S_{max} is the spin size of the HS state ($S_{max} = 5$ for **1**; $S_{max} = 4$ for **2**). $J_{ab}^{(1)}$ corresponds to the case of the weak orbital interaction between magnetic orbitals.[23–25] $J_{ab}^{(2)}$ is applicable in the case of strong orbital interactions.[26,27] $J_{ab}^{(3)}$ has been formulated by using our approximately spin-projected (AP) procedure.[15] The strength of the orbital overlap varies $J_{ab}^{(3)}$ from $J_{ab}^{(1)}$ to $J_{ab}^{(2)}$. Therefore, $J_{ab}^{(3)}$ involves $J_{ab}^{(1)}$ and $J_{ab}^{(2)}$ as weak and strong correlation limits, respectively.

Natural Orbitals and Occupation Numbers. The singly occupied MOs (SOMOs) were nearly degenerate in energy because of long Fe–Fe distances. Since it is hard to analyze the BS SOMOs, we utilized singly occupied NOs (SONOs) holding orbital symmetry, which were determined from the BS SOMOs, in order to understand the origin of the magnetic couplings and the nature of the chemical bonds in **1** and **2**. The NOs of UHF and UDFT solutions can be determined by diagonalizing their first-order density matrices:[28]

$$\rho(\mathbf{r},\mathbf{r}') = \sum n_i \phi_i^*(\mathbf{r})\phi_i(\mathbf{r}'), \tag{2}$$

where n_i denotes the occupation number of NO ϕ_i. The occupation numbers of bonding and antibonding NOs were close to 2.0 and 0.0, respectively, except for ten SONOs of **1** and eight SONOs of **2**, of which the occupation numbers were close to 1.0.

Chemical Indices. Several chemical indices[29,30] were introduced with the occupation numbers of NOs in order to investigate the character of the chemical bonding in the active sites of both oxy and deoxyHr. Effective bond order[29] of the κ-type (σ-type, π-type, and δ-type) was defined by using the occupation number of the bonding NO, $^{\kappa}n_i$, and the antibonding NO, $^{\kappa}n_i{}^*$, as

$$^{\kappa}b_i = \frac{^{\kappa}n_i - {}^{\kappa}n_i^*}{2}. \tag{3}$$

It varied from zero to one, depending on the strength of covalent bonds.

Information entropies have been well defined in several different fields. In chemistry, information entropy (I)[31] is employed to express the characteristic of chemical bonds. The normalized Jaynes information entropy is defined as a measure of chemical bonds by the occupation number of bonding SONOs:

$$^{\kappa}I_i^n = \frac{2\ln 2 - {}^{\kappa}n_i \ln {}^{\kappa} n_i}{2\ln 2} \quad (0 \le {}^{\kappa} I_i^n \le 1). \tag{4}$$

The value of $^{\kappa}I_i^n$ indicates the loss of covalent bonding since $2\ln 2$ corresponds to the maximum entropy of closed-shell bond in this normalized form.

The diradical character ($^{\kappa}y_i^n$) of a chemical bond i is defined by the weight of the doubly excited configuration (W_D) as

$$^{\kappa}y_i^n = 2W_D = 1 - \frac{2^{\kappa}T_i}{1 + (^{\kappa}T_i)^2} = \frac{(^{\kappa}n_i)^2 - 4^{\kappa}n_i + 4}{(^{\kappa}n_i)^2 - 2^{\kappa}n_i + 2}. \tag{5}$$

There are several SONOs in diiron complexes. Therefore, we defined the average normalized indices to investigate the σ-, π-, and δ-type chemical bonding for UDFT:

$$^{\kappa}I^{Ave} = \frac{1}{N}\sum_{i=1}^{N} {}^{\kappa}I_i^n, \tag{6a}$$

$$^{\kappa}Y^{Ave} = \frac{1}{N}\sum_{i=1}^{N} {}^{\kappa}y_i^n, \tag{6b}$$

where N is the number of κ-type orbitals.

Symmetry-adapted (SA) CASCI and CASSCF, followed by the second-order perturbation correction, are desirable for quantitative theoretical treatment of the multinuclear transition-metal complexes in biological systems. However, such computations are difficult to apply to such large systems.[32] For example, we should perform CASCI and CASSCF calculations[33] using a 20-electron and 16-MO active space, which consists of four σ-, four π-, three $\pi_\perp$-, three δ-, and two $\delta_\perp$-orbitals, on **1** and **2**. In this study, we estimated the effective bond orders, the information entropies, and the diradical characters with BS methods, such as UHF and UDFT, to investigate the nature of the chemical bonds in **1** and **2**. These chemical indices can also be calculated with SA methods, because we can compute the occupation numbers of NO using SA methods. The chemical indices are, therefore, common bridges between SA and BS methods.

Computational Procedure

UHF, pure DFT (UBLYP), and hybrid DFT (UB2LYP, UB3LYP, and UB3LYP*) calculations were performed on models of oxy and deoxyHr with the Tatewaki–Huzinaga MIDI (533(21)/53(21)/(41))[34] basis sets plus Hay's d diffuse function ($\alpha = 0.1215$)[35] for Fe, Pople's 6-31G*[36] for C, O, and N, and 6-31G[37] for H.[38] All computations were carried out with the Gaussian03 program packages.[39]

We used realistic models of Hr to investigate the origin of the magnetic couplings, the nature of the chemical bond, and the dioxygen binding mechanism, according to the previous study of Hc.[19] In the models, the five His residues (His25, His54, His73, His77, and His101) coordinated to the Fe ions

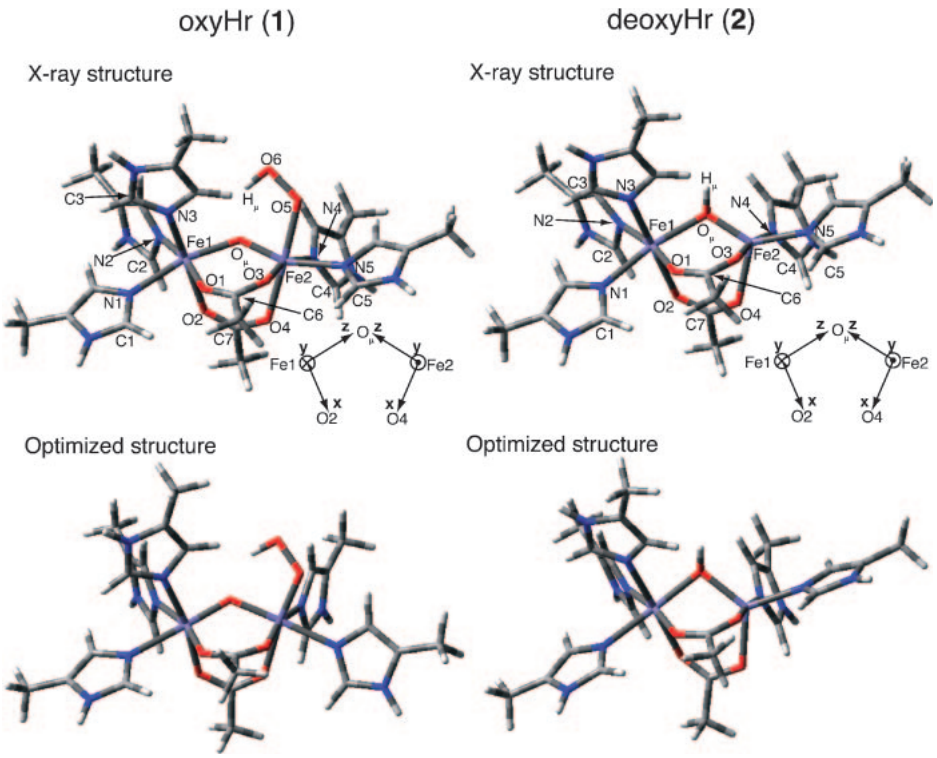

Fig. 2. X-ray and optimized structures of models of **1** and **2** and local coordinate systems centered on Fe1 and Fe2 used to describe the atomic and molecular orbitals. Atom sites are illustrated in **1** and **2**.

in the active site were substituted with neutral methylimidazole, and the bridging Glu58 and Asp106 were replaced with acetate ions as shown in Fig. 2. The geometrical parameters were taken from the X-ray crystallographic studies of oxyHr and deoxyHr.[3,4] In the model of oxyHr, **1**, proton H4 was placed on the binding oxygen to form hydroperoxide, and the location of the proton was optimized. In the model of deoxyHr, the proton (H4) was located at bridging oxygen O3 to form hydroxide. Full geometry optimizations of **1** and **2** were also performed in high- and low-spin states by using the UB2LYP method. The optimized structures were characterized by using harmonic frequency calculations. We compared the geometries, magnetic coupling, and nature of chemical bonds of the optimized structures to those of the X-ray structures. This comparison would provide useful insights about the effects of the protein surrounding the active site on the electronic structures of the active sites.

We calculated the J_{ab} values for **1** and **2** with Eqs. 1a–1c to estimate the magnetic coupling constants and to determine the appropriate DFT functional. Next, the occupation numbers and chemical indices were evaluated using Eq. 2 with the appropriate DFT method. Finally, the ionization potentials of electron-donating orbitals were calculated in order to estimate the charge-transfer interactions between molecular oxygen and Hr. In addition, we analyzed the ionization potentials using Mulliken charge-transfer theory in order to understand the mechanism of the dioxygen binding process in Hr.

Magnetic Interaction for 1 and 2

Comparison between X-ray Structures and Optimized Structures. X-ray and optimized geometrical parameters are shown in Table 1. The deviation of the Fe–N, Fe–O, and O–O bond lengths and the Fe1–O_μ–Fe2 angle of the optimized structures from the X-ray structures of both **1** and **2** were small

Table 1. Selected Geometrical Parameters for OxyHr (**1**) and DeoxyHr (**2**)

	oxy (**1**)		deoxy (**2**)	
	X-ray[a)]	opt[b)]	X-ray[a)]	opt[b)]
Fe1–Fe2[c)]	3.29	3.21	3.34	3.19
Fe–N[c),d)]	2.19	2.21	2.22	2.23
Fe–O[c),e)]	2.18	2.09	2.20	2.15
Fe1–O_μ[c)]	1.94	1.76	2.16	2.05
Fe2–O_μ[c)]	1.66	1.89	1.78	1.98
Fe–OO[c)]	2.19	1.88		
O–O[c)]	1.48	1.42		
∠Fe–O_μ–Fe[f)]	132	125	116	110
d(O_μ–Fe1–N1–C1)[g)]	33.4	−128	38.9	−88.0
d(O_μ–Fe1–N2–C2)[g)]	103	98.1	103	93.1
d(O_μ–Fe1–N3–C3)[g)]	156	174	154	138
d(O_μ–Fe2–N4–C4)[g)]	−148	−107	−160	−151
d(O_μ–Fe2–N5–C5)[g)]	107	71.7	113	100
d(O_μ–Fe1–O1–C6)[g)]	−5.26	−8.50	−11.9	−13.4
d(O_μ–Fe1–O3–C7)[g)]	30.5	32.2	44.1	65.2

a) The parameters are taken from the X-ray structure of oxyHr (1HMO) and deoxyHr (1HMD). b) The parameters were fully optimized at the UB2LYP level of theory. c) Distances are given in angstroms. d) Average value for bond distances between Fe and Nε of the His coordinated to Fe. e) Average value for bond distances between Fe and Oγ of the Asp or Glu coordinated to Fe. f) Angles are given in degrees. g) Dihedral angles are given in degrees.

(less than 0.1 Å and about 10°). Although the Fe–Fe distance in **1** was 3.21 Å, which is in good agreement with the crystallographic and EXAFS study (3.24 Å),[40] the Fe–Fe distance in **2** was shorter than that in the X-ray structure (3.34 Å) and the EXAFS data (3.57 Å). This deviation in the calculated Fe–Fe distance in **2** from the EXAFS study has also been reported by Wirstam et al.[13] The similarity of the optimized Fe–Fe and O–O bond lengths in **1** to those in the X-ray structure of oxyHr shows that the proton is transferred to dioxygen to form hydroperoxide upon the reaction of **1** with an oxygen molecule. During the geometry optimization, the difference between the Fe1–O_μ and Fe2–O_μ bond lengths changed from 0.28 and 0.38 Å to −0.1 and 0.1 Å for **1** and **2**, respectively, indicating that the asymmetrical structures of the diiron core relaxed. Other discrepancies between the optimized structures and the X-ray structures were the dihedral angles of the imidazole rings of the histidine residues, as shown in Table 1. These deviations presumably imply that the protein structure keeps the active site in specific positions.

Effective Exchange Integrals. In order to determine the appropriate DFT method, we calculated the values of J_{ab} for **1** and **2**. Table 2 summarizes the J_{ab} values for **1** and **2** by using Eqs. 1a–1c. All of the calculated values of J_{ab} show antiferromagnetic couplings between the Fe ions, which is qualitatively consistent with experimental results.[3–6] The absolute values of the J_{ab} for **1** and **2** were underestimated using UHF calculations in comparison to the experimental values, whereas they were overestimated using UBLYP calculations. Brunold and Solomon[6] have also reported that $|J_{ab}|$ values ($-214\,cm^{-1}$) for $[(NH_3)_3Fe(\mu\text{-}O)(\eta^2\text{-}HCOO)_2Fe(OOH)(NH_3)_2]$ were too large, similar to the value ($-396.1\,cm^{-1}$) we obtained using UBLYP calculations, indicating that pure DFT calculations tend to estimate absolute values of J_{ab} that are much larger than the experimental values. On the other hand, the J_{ab} values for **1** and **2** calculated by using hybrid DFT (HDFT) methods, such as UB2LYP and UB3LYP calculations, were close to the experimental values quantitatively. In particular, UB2LYP exchange-correlation functional, which contains 50% HF exchange, was the most reliable for determining the magnetic couplings and the electronic structures of oxyHr and deoxyHr. The experimental magnetic coupling constants could not be reproduced using UB3LYP*, because this functional includes only 15% HF exchange.

Table 2. Magnetic Coupling Constants (J_{ab})[a] Calculated for the Models of OxyHr (**1**) and DeoxyHr (**2**)

Model	Method	$J_{ab}^{(1)}$	$J_{ab}^{(2)}$	$J_{ab}^{(3)}$
1[b]	UHF	−14.10	−11.75	−14.09
	UB2LYP	−49.18	−40.98	−48.95
	UB2LYP (opt)[d]	−53.95	−44.96	−53.78
	UB3LYP	−148.4	−123.7	−145.1
	UB3LYP*	−170.5	−142.1	−166.0
	UBLYP	−413.3	−344.4	−396.1
2[c]	UHF	−3.492	−2.794	−3.492
	UB2LYP	−10.38	−8.300	−10.37
	UB2LYP (opt)[d]	−6.674	−5.339	−6.672
	UB3LYP	−22.84	−18.27	−22.81
	UB3LYP*	−27.22	−21.78	−27.17
	UBLYP	−25.96	−20.76	−25.76

a) J_{ab} are shown in cm^{-1}. b) $J_{ab}(exp.) = -77\,cm^{-1}$ for oxyHr. c) $J_{ab}(exp.) = -14\,cm^{-1}$ for deoxyHr. d) Geometrical parameters were fully optimized.

By using Eqs. 1a–1c, the strength of the orbital overlap of the SOMOs can be obtained quantitatively.[30] The $J_{ab}^{(3)}$ values determined by using our AP procedure were close to $J_{ab}^{(1)}$ for **1** and almost the same for **2**. The absolute values of the J_{ab} is in the order $|J_{ab}^{(2)}| < |J_{ab}^{(3)}| \leq |J_{ab}^{(1)}|$ for **1** and $|J_{ab}^{(2)}| < |J_{ab}^{(3)}| \approx |J_{ab}^{(1)}|$ for **2**. This result indicates that **1** and **2** have weak-overlap and no-overlap, respectively. This clearly shows that comparisons of $J_{ab}^{(p)}$ ($p = 1$–3) are promising for elucidating the orbital overlap effect on the SE interaction.

The differences in the J_{ab} values between the X-ray structures and the optimized structures were small (about 5 cm^{-1}). This is because the total Fe–O_μ bond lengths (Fe1–O_μ + Fe2–O_μ), namely, the distance between Fe1 and Fe2 via the O_μ site, are almost same between the X-ray structure (3.6 Å in **1** and 3.94 Å in **2**) and the optimized structure (3.65 Å in **1** and 4.03 Å in **2**), though the shape of the diiron core changed during geometry optimization. On the other hand, the large discrepancy in the Fe–Fe distance were hardly reflected in the J_{ab} values, indicating that the direct interaction of the Fe sites slightly contributes to the magnetic couplings of **1** and **2**.

Charge and Spin Density Populations. We investigated the charge and spin density populations of **1** and **2** to elucidate the characteristics of the CTs among Fe^{III} (or Fe^{II}), O^{2-} (or OH^-), and ligands. In Table 3, the charge density on the O_μ site in **1** varied from a formal charge of −2.0 to about −1.0, and that on the hydroxide group ($O_\mu H_\mu$) in **2** changed from formal charge of −1.0 to about −0.5, indicating the back CT to the Fe ions for both models. The back CT implies that SE interactions are responsible for the antiferromagnetic cou-

Table 3. Charge and Spin Densities for **1** and **2** Determined by Using UB2LYP in the LS State

Model			Fe1[a]	Fe2[a]	O_μ[a]	H_μ[a]	O5[a]	O6[a]
1	X-ray	Charge	1.394	1.457	−1.009	0.472	−0.473	−0.558
		Spin	4.310	−4.228	0.026	0.001	−0.206	−0.011
	opt[b]	Charge	1.525	1.492	−1.062	0.485	−0.546	−0.486
		Spin	4.282	−4.280	0.209	0.000	−0.280	−0.022
2	X-ray	Charge	1.100	1.113	−1.042	0.436		
		Spin	3.850	−3.793	−0.061	−0.005		
	opt[b]	Charge	1.120	1.058	−0.878	0.466		
		Spin	3.841	−3.831	−0.012	0.001		

a) The atom sites are shown in Fig. 2. b) Geometrical parameters were fully optimized.

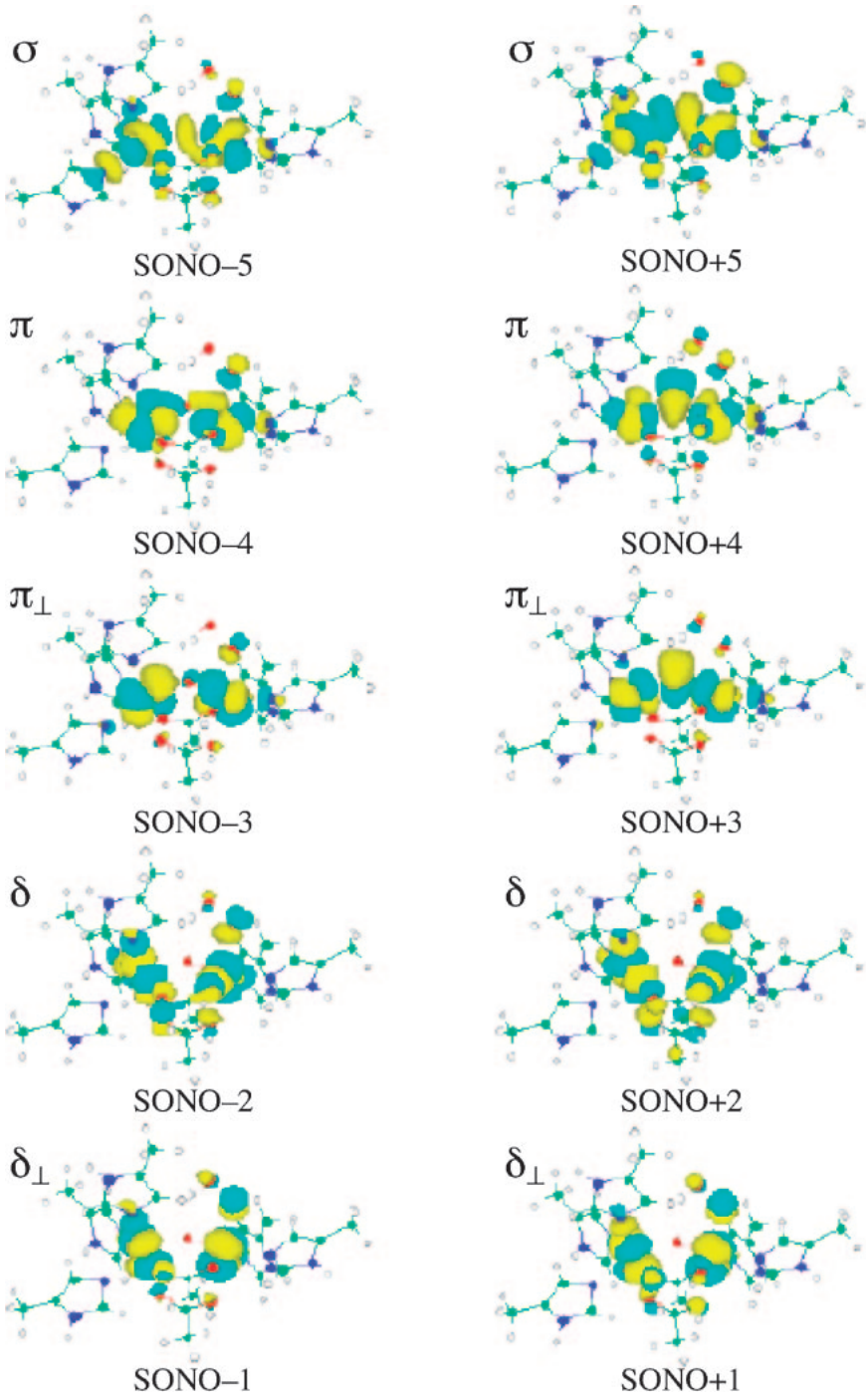

Fig. 3. Bonding (SONO−5 to SONO−1) and antibonding (SONO+1 to SONO+5) singly occupied natural orbitals (SONOs) for the LS state of **1** at the UB2LYP level of theory.

pling in Hr. The ligands regulate the back CT from the μ-O or μ-OH group to the Fe–Fe core, namely, charge delocalization on the active site. The charge densities of the OOH part (O5 + O6 + H_μ) in **1** are about −1.0, showing that the charge densities of the active site are transferred to the O5 and O6 sites when dioxygen is bound to the active core of **1** and a proton in the active core moves to the dioxygen.

The spin densities calculated by using UB2LYP were delocalized over the Fe(μ-O)Fe and Fe(μ-OH)Fe sites. The computed spin densities on the Fe^{III} ions of **1** and the Fe^{II} ions of **2** are typical for binuclear Fe^{III} or Fe^{II} complexes.[11,41] Since the spin densities on the O_μ site of **1** and $O_\mu H_\mu$ part of **2** in the X-ray structure were so small, spin polarization effects should not influence the magnetic coupling for Hr. The spin densities on O5 and O6 of **1** were about 0.0. Judging from the charge and spin densities, dioxygen takes two electrons and one proton and becomes a hydroperoxide ion, OOH^-.

The charge and spin densities of the optimized structures were similar to those of the X-ray structures, except for the spin density on the O_μ site of **1**, due to the structural difference

in the diiron core. Wirstam et al. have also reported a similar spin density on the O_μ site of **1** during the geometry optimization.[13] It might be necessary to perform additional experiments and calculations in order to determine whether the appearance of the radical character of the bridging μ-O group is artificial or not.

The Nature of the Chemical Bonds

Natural Orbital Analysis. The bonding and antibonding SONOs and the occupation numbers should clarify the origin of the magnetic couplings in **1** and **2**. Figure 3 illustrates the SONOs of **1** in the LS state determined by using UB2LYP calculations. SONO−5 and SONO+5 showed σ-type ($d\sigma$–$p\sigma$–$d\sigma$) interactions consisting of d_{z^2} orbitals of the Fe ions and vacant 3s orbital (SONO−5) or filled 2p orbital (SONO+5) of the μ-O group. SONO−4, SONO+4, SONO−3, and SONO+3, had π-type ($d\pi$–$p\pi$–$d\pi$) interactions. SONO−4 and SONO+4 formed via orbital interactions between the d_{xz} orbitals of the Fe ions and filled 2p orbitals of the μ-O group. SONO−3 formed via orbital interaction of the d_{yz} orbitals of the Fe ions, and SONO+3 formed by overlap between the d_{yz} orbitals of Fe ions and 2p orbital of the μ-O group. SONO−2, SONO+2, SONO−1, and SONO+1 showed δ-type ($d\delta$–$d\delta$) interactions, in which the $d_{x^2-y^2}$ or d_{xy} orbitals of the Fe ions interact with each other via the bridging acetate ligand. We observed that the σ- and π-type SONOs were delocalized across the Fe(μ-O)Fe site and that δ-type SONOs were delocalized over the Fe(μ-$OOCH_3$)Fe at the UB2LYP level. The delocalized orbitals can be explained by the antiferromagnetic SE interactions between the Fe ions. These results indicate that the orbital interactions via the μ-O and acetate group are involved in the antiferromagnetic coupling between the two ferric ions in **1**.

For **2**, SONO−4 and SONO+4 showed σ-type interactions of the Fe ions via the μ-OH group, and SONO−3, SONO+3, SONO−2, and SONO+2 involved π-type interactions of the Fe ions through the μ-OH group. SONO−1 and SONO+1 showed δ-type interactions of the Fe ions via the acetate group, as illustrated in Fig. 4. The SONOs were found to be delocalized on the Fe(μ-OH)Fe and Fe(μ-$OOCH_3$)Fe sites, leading to antiferromagnetic SE interaction between the Fe ions, indicating that the orbital interactions via μ-OH and acetate groups give rise to the antiferromagnetic coupling between the two ferrous ions in **2**.

Chemical Indices. Since magnetic couplings are largely related to the nature of the chemical bond, we discuss here the characteristics of the chemical bond in both oxyHr and deoxyHr. Table 4 lists the occupation numbers of SONOs for **1** and **2**. We can estimate the effective bond order, b, using the occupation numbers of SONOs with Eq. 3. For the X-ray structures, the values of b were estimated to be 0.23 (σ), 0.16 (π), 0.14 ($\pi_\perp$), 0.02 (δ), and 0.01 ($\delta_\perp$) for **1**, and 0.12 (σ), 0.07 (π), 0.04 ($\pi_\perp$), and 0.01 (δ) for **2** at the UB2LYP level of theory. The d–p interactions of the active site become stronger in the order $\sigma > \pi \gg \delta$, indicating that the σ- and π-type orbital interactions mainly contribute to the magnetic couplings in **1** and **2**. It is known that Fe–O bond lengths correlate with the strength of antiferromagnetic coupling and that the magnitude of that coupling decays with an increase in the distances.[42] Since the Fe–O_μ bond distances are shorter than the Fe–O(acetate) bond distances, the σ- and π-type orbital interactions are stronger than the δ-type orbital interactions.

The effective bond orders of σ- and π-type SONOs for **1** were larger than those for **2** by 0.1, showing the same tendency as the J_{ab} values. This implies that the σ- and π-type orbital interactions in **2** are much smaller than those in **1**. The small magnetic coupling constant for **2** is due to small SE interactions. On the other hand, b of the δ-type SONOs for **1** and **2** are similar to each other, also implying that the δ-type orbital interaction through acetate groups is not responsible for the difference in the magnetic couplings between oxyHr and deoxyHr. The occupation numbers of the HOMO and LUMO were 1.997 and 0.003 for **1** and 1.998 and 0.002 for **2** by using UB2LYP, respectively, showing that the spin polarization effect is much smaller than the σ- and π-type orbital interactions. NO analysis clearly demonstrates that the origin of the antiferromagnetic couplings in Hr is the σ- and π-type orbital interactions via the weak Fe–O conjugation (σ- and π-type SE interactions).

The information entropy (I) and diradical character (Y) are also useful indices for the investigation of the character of the chemical bond.[43] Using the occupation numbers of the SONOs, the indices were estimated using Eq. 6. In Table 5, the values of I express the loss of the covalency of the chemical bonds, and the values of Y, which characterize the double excitation of the electrons occupying the bonding NOs, indicate how much the unpaired electrons can localize on the spin sites. They can be regarded as useful indices to diagnose the bond nature and measures of the strength of orbital interactions. Previously, we have investigated the nature of the chemical bonds of organic systems, showing that intermolecular radical character of organic radicals, phenalenyl radical dimeric pair, has an I value of 0.65 and a Y value of 0.30.[30] In comparison with the organic system, we found that spin sites in **1** show strong radical character, that is, rather weak orbital interactions; however, the weak bond character is sufficient for cooperative intramolecular (through-bond) charge transport for the proton migration step of the oxygen trapping (see below), namely, the reversible dioxygen binding in Hr. **2** belongs to the very weak orbital interaction region, showing small antiferromagnetic coupling.

The information entropies and diradical characters of **1** were related to the orbital type in the following order: $\sigma < \pi < \delta$. All of the δ-type information entropies and diradical characters were almost 1.0, showing that the complete loss of the covalency of the δ-type orbital interactions between the Fe^{III} ions via the bridging acetate ligands and that the unpaired electron in $d_{x^2-y^2}$ or d_{xy} orbital is almost localized on the Fe sites. The σ- and π-type information entropies and diradical characters were less than 1.0, implying that the Fe–O_μ bonds have some covalency and that the unpaired electron in d_{z^2}, d_{zx}, or d_{zy} orbital is slightly delocalized over the diiron core in the active site. The σ-, π-, and δ-type chemical indices for **2** were almost 1.0, which shows that the unpaired electrons in the d orbitals are localized on the Fe^{II} sites, resulting in the weak antiferromagnetic SE interactions in **2**.

The optimized structure afforded smaller σ- and π-type chemical indices for both **1** and **2** than those of the X-ray struc-

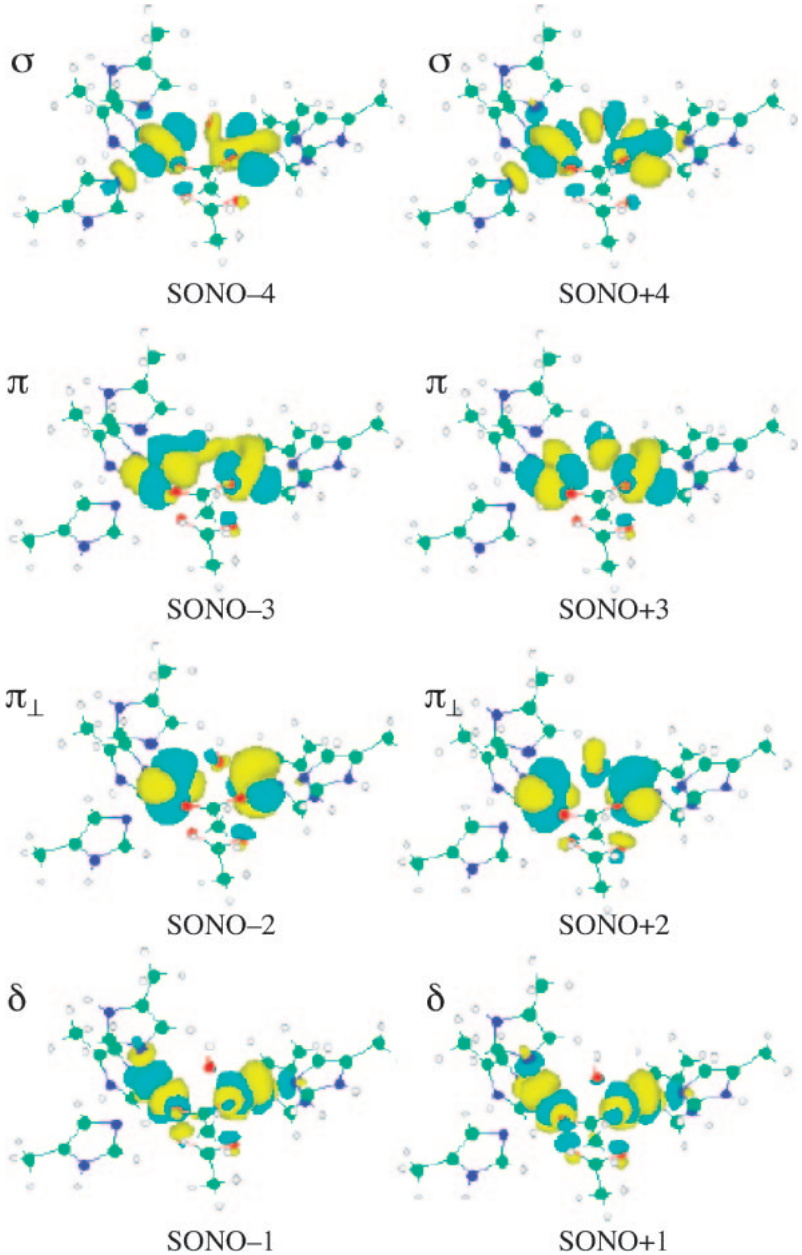

Fig. 4. Bonding (SONO−4 to SONO−1) and antibonding (SONO+1 to SONO+4) singly occupied natural orbitals (SONOs) for the LS state of **2** at the UB2LYP level of theory.

Table 4. Occupation Numbers[a)] of HOMO and SOMOs (SONOs) of **1** and **2** by UB2LYP in the LS State

Model		HOMO	SOMO−5	SOMO−4	SOMO−3	SOMO−2	SOMO−1
1	X-ray	1.997	1.228	1.163	1.142	1.016	1.010
	opt[b)]	1.997	1.183	1.135	1.121	1.016	1.012
2	X-ray	1.998		1.120	1.073	1.043	1.012
	opt[b)]	1.997		1.056	1.031	1.018	1.005

a) n(SOMO−p) + n(SOMO+p) = 2.0 and n(HOMO) + n(LUMO) = 2.0. b) Geometrical parameters were fully optimized.

ture, due to the relaxation of the Fe–O_μ bond lengths. It indicates that the protein environment causes σ- and π-type orbital interactions in the diiron core to become stronger in the active site of oxyHr and deoxyHr.

Charge-Transfer Mechanism for Dioxygen Trapping

One-Electron-Transfer Step. The orbital energy levels determined by using UB2LYP were utilized to depict the

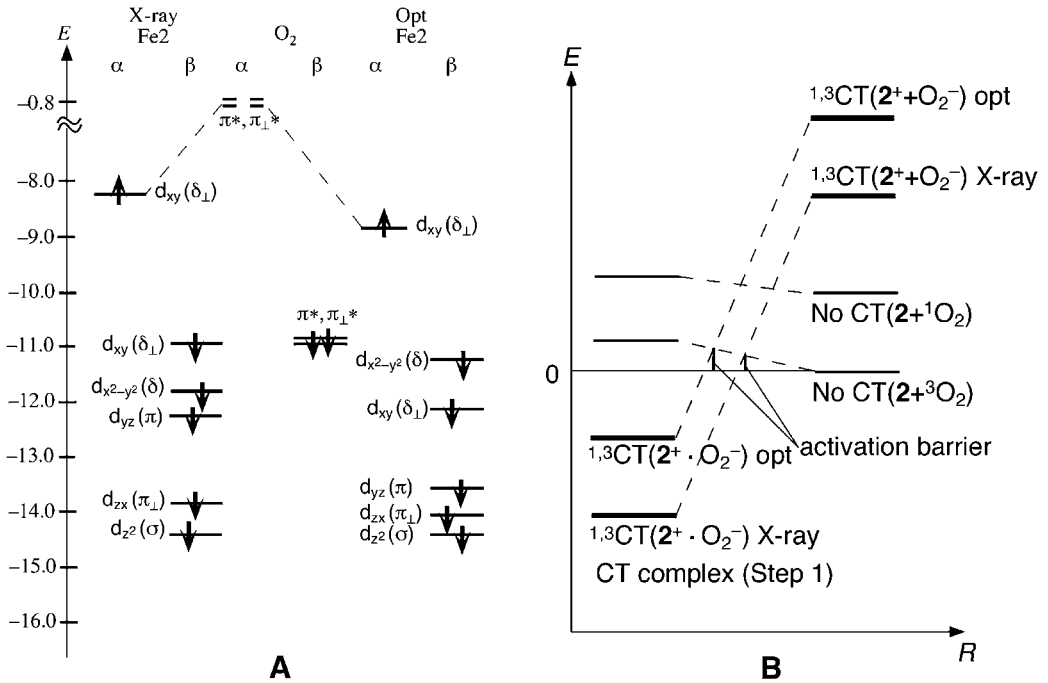

Fig. 5. Orbital energy diagrams of the d orbitals at the Fe2 ion of **2** and the π^* and $\pi_\perp{}^*$ orbitals of dioxygen at the UB2LYP level of theory (**A**) and configuration energy diagrams determined by using the Mulliken CT theory (**B**).

Table 5. Chemical Indices such as Information Entropy, I, and Diradical Character, Y, for σ-, π-, and δ-Type Orbitals of **1** and **2** Determined by Using UB2LYP in the LS State

Model		κ	κI^{Ave}	κY^{Ave}
1	X-ray	σ-type	0.818	0.567
		π-type	0.882	0.701
		δ-type	0.991	0.974
	opt[a)]	σ-type	0.856	0.645
		π-type	0.902	0.748
		δ-type	0.990	0.972
2	X-ray	σ-type	0.954	0.876
		π-type	0.979	0.942
		δ-type	0.996	0.990
	opt[a)]	σ-type	0.958	0.888
		π-type	0.982	0.951
		δ-type	0.997	0.991

a) Geometrical parameters were fully optimized.

CT excitation energy diagrams and possible potential energy curves. Using the orbital energy of the Fe–Fe site in **2** and dioxygen, we discuss the mechanism of the dioxygen binding of Hr qualitatively. When dioxygen becomes close to the active core in Hr, it binds to the Fe2 site. The orbital energies of the d orbitals of Fe2 and the π and $\pi_\perp$ orbitals of O_2 are shown in Fig. 5A. From Fig. 5A, the different coordination number and the strong electron correlation effects on the Fe ions cause these large energy gaps between the α and β d_{xy} orbitals. This indicates that dioxygen binds stepwise to **2**, as illustrated in Fig. 6A. From UB2LYP calculations, only the α orbital energies of the d_{xy} orbital of Fe2 in both the X-ray structure (−8.27 eV) and the optimized structure (−8.83 eV) are the closest to that of the $\pi_\perp{}^*$ orbitals in O_2 (−0.81 eV), implying that the d_{xy} orbital of Fe2

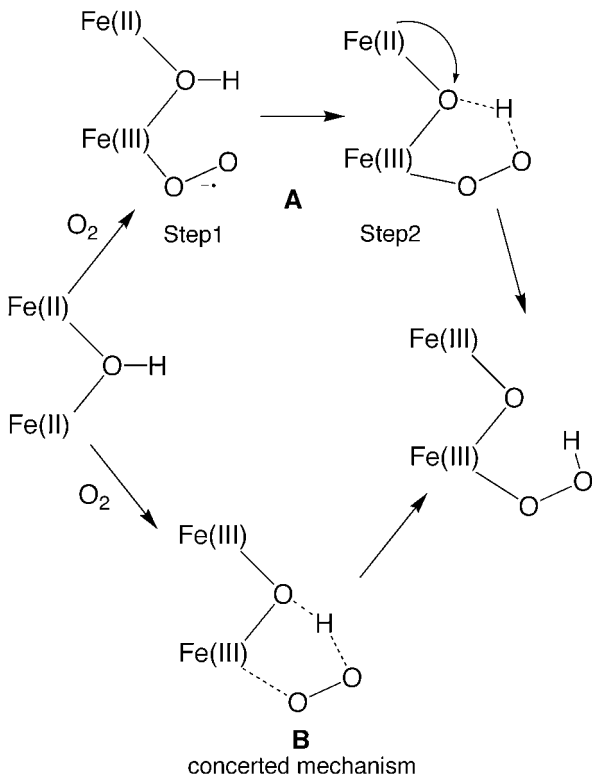

Fig. 6. Proposed two-step (**A**) and one-step (**B**) mechanisms for dioxygen binding to Hr based on experimental observations.

interacts with the $\pi_\perp{}^*$ orbitals of O_2 when dioxygen approaches the active site in Hr. The CT should occur from the d_{xy} orbital of Fe2 to the $\pi_\perp{}^*$ orbital of O_2 when dioxygen is bound to the Fe2 site in Hr, resulting in a mixed-valence

(MV) $Fe^{II}1$–$Fe^{III}2$ core and O_2^- anion (Step 1 as shown in Fig. 6A).

We also compared the orbital energies estimated for the X-ray structure to those for the optimized structure in order to obtain insights about the effects of the different shapes of the diiron core and the conformation of the ligands, such as His, Asp, and Glu, on the dioxygen binding process of Hr. The highest α orbital energy of Fe2 (d_{xy} orbital) in the X-ray structure was closer to the $\pi_\perp^*$ orbitals of O_2 than that in the optimized structure, that is, the d_{xy} orbital of Fe2 in **2** could interact with the $\pi_\perp^*$ orbitals of O_2 more strongly in the X-ray structure than in the optimized structure. The structural deformation of the active site by the surrounding protein could strengthen the orbital interaction of the Fe2 site and oxygen molecule. However, it is difficult to estimate the binding free energy of oxygen molecule to Hr accurately, because explicit treatment of the surrounding protein and long MD simulation to sample the whole phase space are required.

From Mulliken CT theory,[21] the weight of the CT configuration is essentially determined by the energy gap between the ground and CT configurations, which are parallel to the ionization potential. The CT excitation energy from the d_{xy} orbitals in **2** for the X-ray structure to the $\pi_\perp^*$ orbital of O_2, which affords a CT ($\mathbf{2}^+ + O_2^-$) state, is smaller than that for the optimized structure, leading to the larger stabilization energy by configuration mixing between CT ($\mathbf{2}^+ + O_2^-$) and non-CT ($\mathbf{2} + O_2$) states. Such strong CT interactions between **2** in the X-ray structure and dioxygen could be the origin of the smaller activation barrier of **2** in the X-ray structure than that in the optimized structure, as shown in Fig. 5B.[21]

Spin Inversion and Oxygen Activation. As shown in Fig. 5B, the spin state of the initial complex between **2** and $^3O_2$ is a triplet state, because the ground state of **2** is a singlet state, indicating that the spin inversion from the triplet to the singlet state occurs to afford the singlet **2-O$_2$** complex. From Fig. 5B, the initially formed CT complex between the MV [Fe^{II}–Fe^{III}] core and $O_2^{-\bullet}$ is possibly a triplet state; however, the energy gap between the triplet and singlet CT complexes could be smaller than that between non-CT complexes ($\mathbf{2} + {}^1O_2$ and $\mathbf{2} + {}^3O_2$), because the complexes consist of magnetically coupled species. This implies facile spin inversion from the triplet to the singlet state within the CT complex: $\{{}^2[Fe^{II}\text{–}Fe^{III}]\cdot{}^2[O_2^-]\}$. Probably, protein dynamics play important roles in the process, especially in Step 2, with respect to the cooperative proton- and electron-transfer (PET) reaction, as illustrated in Fig. 6A.

Judging from the CT excitation energies, coordination effects of the ligands will influence the function of the protein. For example, although the geometric structures of the active cores in MMO (Fig. 1B), which catalyzes the conversion of methane to methanol, and RNR (Fig. 1C), which catalyzes the reduction of ribonucleotides to their corresponding deoxyribonucleotides, are similar to that of Hr, their functions are different from that of Hr. The functions of MMO and RNR are attributed to the non-bridging carboxylate ligands, utilized instead of imidazole ones. The electron-donating character of the carboxylate is stronger than that of the imidazole, leading to the increase in the orbital energy corresponding to the Fe site near the π^* or σ^* orbitals of O_2. The strong electron donation could result in the breaking of the O–O bond and oxygen activation. If we can change the ligands from $HBpz_3$ to more electron-donating ligands, as shown in Fig. 1A(c), the complex may show oxygenase function.

One- or Two-Step Mechanism for Oxygen Trapping. Both one- and two-step mechanisms have been proposed to explain the oxygen-trapping process in Hr on the basis of the experimental evidence, as illustrated in Fig. 6. Howard and Rees[44a] have proposed a mechanism consisting of two one-electron transfers bracketing proton transfer from the metal center to the dioxygen, as illustrated in Fig. 6A (two-step mechanism). Que and True[44b] have proposed a mechanism with proton transfer following a concerted two-electron transfer, as shown in Fig. 6B (one-step mechanism). In this study, the α orbital energies of Fe1 and Fe2 in **2** were -10.8 and -8.27 eV, respectively, because of the difference in the coordination number of the Fe ions, showing that the simultaneous two-electron transfer is difficult from **2** to dioxygen. This result supports the two-step mechanism shown in Fig. 6A. Our two-step CT mechanism indicates that spin inversion from the triplet state to the singlet state occurs in Step 1, namely the one-electron-transfer step, and then, the cooperative PET step (Step 2) takes place without spin inversion. However, to confirm this proposal, it is necessary to analyze the potential energy surface and the variation in the charge and spin densities in the dioxygen binding process of deoxyHr in more detail.

In this study, we found that UB2LYP with our AP scheme is a reliable procedure to investigate the electronic structure of oxyHr and deoxyHr. Our AP scheme is also applicable to broken-symmetry solutions, for which the orbital overlaps (T_i) between magnetic orbitals are not negligible. The total energy in the pure LS state is given by the AP scheme[19,45,46] as

$$^{\text{AP-LS}}E_{\text{X}} = {}^{\text{LS}}E_{\text{X}} + J_{\text{ab}}^{(3)}[{}^{\text{LS}}\langle S^2\rangle - S_{\min}(S_{\min}+1)], \qquad (7)$$

where $S_{\min}$ is the spin angular momentum of the LS state. This equation removes a major portion of the errors caused by spin contamination, making it possible to depict the potential energy curves, as shown previously.[19] In fact, Equation 7 works well in the entire region of the dissociation processes of covalent bonds, since the AP-LS energy reduces to the LS energy of the closed-shell state at the instability threshold of $T_i = 1$.[21] Our AP scheme should be applicable to the investigation of the PET step.

Concluding Remarks

We performed UHF and UDFT calculations on **1** and **2** to investigate the magnetic interaction and the nature of the chemical bonds in oxyHr and deoxyHr. Our conclusions are as follows: (i) Since hybrid DFT, especially UB2LYP, can reproduce the experimental values quantitatively, UB2LYP can be regarded as a reliable method for the investigation of the magnetic coupling constant of both oxyHr and deoxyHr. (ii) σ- and π-type orbital interactions via the μ-OH bridge account for the weak antiferromagnetic interaction between the two ferrous ions in deoxyHr. (iii) σ- and π-type orbital interactions via the μ-O bridging atom are responsible for the antiferromagnetic coupling between the two ferric ions in oxyHr. (iv) The difference in $d\sigma$–$p\sigma$ and $d\pi$–$p\pi$ interactions of the active core correlate with the difference in the magnetic coupling

constants between oxyHr and deoxyHr. (v) Analysis of the ionization potential based on the Mulliken CT theory indicates that the dioxygen binding in Hr proceeds through a two-step electron-transfer mechanism. (vi) Hybrid DFT calculations, followed by chemical bond analyses, are applicable to other binuclear transition-metal complexes found in enzymes.[47–49]

We would like to thank Dr. Andrew G. Leach for helpful discussion. We are grateful to the Japan Society for the Promotion of Science for a Research Fellowship for Young Scientists and to the Ministry of Education, Culture, Sports, Science and Technology (MEXT) Japan for the Grant-in-Aid for Scientific Research on Priority Areas "Structures of Biological Macromolecular Assemblies" (No. 513-18054013) and the Grant-in-Aid for Encouragement of Young Scientists (No. 18750011). The computations were performed using Research Center for Computational Science, Okazaki, Japan and Cybermedia Center at Osaka University, Japan.

Supporting Information

The following data are included: Detailed theoretical background and the total energies and total angular momentums for **1** and **2** by UHF, UB2LYP, UB3LYP, and UBLYP (PDF). This material is available free of charge on the web at http://www.csj.jp/journals/bcsj/.

References

1 R. E. Stenkamp, *Chem. Rev.* **1994**, *94*, 715.

2 a) S. J. Lippard, *Angew. Chem., Int. Ed. Engl.* **1988**, *27*, 344. b) D. M. Kurtz, Jr., *Chem. Rev.* **1990**, *90*, 585.

3 M. A. Holmes, I. Le Trong, S. Turley, L. C. Sieker, R. E. Stenkamp, *J. Mol. Biol.* **1991**, *218*, 583.

4 J. W. Dawson, H. B. Gray, H. E. Hoenig, G. R. Rossman, J. M. Schredder, R. H. Wang, *Biochemistry* **1972**, *11*, 461.

5 R. C. Reem, J. M. McCormick, D. E. Richardson, F. J. Devlin, P. J. Stephens, R. L. Musselman, *J. Am. Chem. Soc.* **1989**, *111*, 4688.

6 T. C. Brunold, E. I. Solomon, *J. Am. Chem. Soc.* **1999**, *121*, 8277.

7 a) W. H. Armstrong, S. J. Lippard, *J. Am. Chem. Soc.* **1983**, *105*, 4837. b) W. H. Armstrong, A. Spool, G. C. Papaefthymiou, R. B. Frankel, S. J. Lippard, *J. Am. Chem. Soc.* **1984**, *106*, 3653. c) P. Chaudhury, K. Wieghardt, B. Nuber, J. Weiss, *Angew. Chem., Int. Ed. Engl.* **1985**, *24*, 778. d) J. R. Hartman, R. L. Rardin, P. Chaudhuri, K. Pohl, K. Wieghardt, B. Nuber, J. Weiss, G. C. Papaefthymiou, R. B. Frankel, S. J. Lippard, *J. Am. Chem. Soc.* **1987**, *109*, 7387. e) M. Kodera, K. Kano, *Bull. Chem. Soc. Jpn.* **2007**, *80*, 662.

8 S. H. Vosko, L. Wilk, M. Nusair, *Can. J. Phys.* **1980**, *58*, 1200.

9 A. D. Becke, *Phys. Rev. A* **1988**, *38*, 3098.

10 J. P. Perdew, *Phys. Rev. B* **1986**, *33*, 8822.

11 J. H. Rodriguez, J. K. McCusker, *J. Chem. Phys.* **2002**, *116*, 6253.

12 J. P. Perdew, Y. Wang, *Phys. Rev. B* **1992**, *45*, 13244.

13 M. Wirstam, S. J. Lippard, R. A. Friesner, *J. Am. Chem. Soc.* **2003**, *125*, 3980.

14 M. Shoji, Y. Nishiyama, Y. Maruno, K. Koizumi, Y. Kitagawa, S. Yamanaka, T. Kawakami, M. Okumura, K. Yamaguchi, *Int. J. Quantum Chem.* **2004**, *100*, 887.

15 a) K. Yamaguchi, Y. Takahara, T. Fueno, in *Applied Quantum Chemistry*, ed. by V. H. Smith, H. F. Schafer, III, K. Morokuma, D. Reidel, Boston, Massachusetts, **1986**, p. 155. b) K. Yamaguchi, H. Fukui, T. Fueno, *Chem. Lett.* **1986**, 625. c) K. Yamaguchi, T. Tsunekawa, Y. Toyoda, T. Fueno, *Chem. Phys. Lett.* **1988**, *143*, 371. d) Y. Takano, T. Soda, Y. Kitagawa, Y. Yoshioka, K. Yamaguchi, *Chem. Phys. Lett.* **1999**, *301*, 309. e) Y. Takano, T. Onishi, Y. Kitagawa, T. Soda, Y. Yoshioka, K. Yamaguchi, *Int. J. Quantum Chem.* **2000**, *80*, 681. f) Y. Takano, Y. Kitagawa, T. Onishi, Y. Yoshioka, K. Yamaguchi, N. Koga, H. Iwamura, *J. Am. Chem. Soc.* **2002**, *124*, 450.

16 A. D. Becke, *J. Chem. Phys.* **1993**, *98*, 5648.

17 A. D. Becke, *J. Chem. Phys.* **1993**, *98*, 1372.

18 C. Lee, W. Yang, R. G. Parr, *Phys. Rev. B* **1988**, *37*, 785.

19 a) Y. Takano, S. Kubo, T. Onishi, H. Isobe, Y. Yoshioka, K. Yamaguchi, *Chem. Phys. Lett.* **2001**, *335*, 395. b) Y. Takano, K. Yamaguchi, *Int. J. Quantum Chem.* **2007**, *107*, 3103.

20 M. Reiher, O. Salomon, B. A. Hess, *Theor. Chem. Acc.* **2001**, *107*, 48.

21 a) K. Yamaguchi, in *Singlet Oxygen*, ed. by A. A. Frimer, CRC Press, Boca Raton, Florida, **1985**, p. 119. b) Y. Takano, T. Tsunesada, H. Isobe, Y. Yoshioka, K. Yamaguchi, I. Saito, *Bull. Chem. Soc. Jpn.* **1999**, *72*, 213.

22 Detailed theoretical background is shown in Supporting Information.

23 A. P. Ginsberg, *J. Am. Chem. Soc.* **1980**, *102*, 111.

24 L. Noodleman, *J. Chem. Phys.* **1981**, *74*, 5737.

25 L. Noodleman, E. R. Davidson, *Chem. Phys.* **1986**, *109*, 131.

26 A. Bencini, F. Totti, C. A. Daul, K. Doclo, P. Fantucci, V. Barone, *Inorg. Chem.* **1997**, *36*, 5022.

27 E. Ruiz, J. Cano, S. Alvarez, P. Alemany, *J. Comput. Chem.* **1999**, *20*, 1391.

28 K. Yamaguchi, M. Okumura, K. Takada, S. Yamanaka, *Int. J. Quant. Chem., Quantum Chem. Symp.* **1993**, *27*, 501.

29 a) H. Isobe, Y. Takano, Y. Kitagawa, T. Kawakami, S. Yamanaka, K. Yamaguchi, K. N. Houk, *Mol. Phys.* **2002**, *100*, 717. b) K. Yamaguchi, in *Self-Consistent Field Theory and Applications*, ed. by R. Carbo, M. Klobukowski, Elsevier, Amsterdam, **1990**. c) M. Nishino, S. Yamanaka, Y. Yoshioka, K. Yamaguchi, *J. Phys. Chem. A* **1997**, *101*, 705. d) H. Isobe, Y. Takano, Y. Kitagawa, T. Kawakami, S. Yamanaka, K. Yamaguchi, K. N. Houk, *J. Phys. Chem. A* **2003**, *107*, 682.

30 a) Y. Takano, T. Taniguchi, H. Isobe, T. Kubo, Y. Morita, K. Yamamoto, K. Nakasuji, T. Takui, K. Yamaguchi, *J. Am. Chem. Soc.* **2002**, *124*, 11122. b) Y. Takano, T. Taniguchi, H. Isobe, T. Kubo, Y. Morita, K. Yamamoto, K. Nakasuji, T. Takui, K. Yamaguchi, *Chem. Phys. Lett.* **2002**, *358*, 17.

31 a) C. E. Shannon, *Bell Syst. Tech. J.* **1948**, *27*, 379. b) C. W. Helstrom, *Quantum Detection and Estimation Theory*, Academic Press, New York, **1976**. c) M. Oya, *IEEE Trans. Inf. Theory* **1983**, *29*, 70. d) E. Jaynes, in *Papers on Probability, Statistics and Statistical Physics*, ed. by R. Rosencrantz, Reidel, Dordrecht, **1993**. e) D. M. Collins, *Z. Naturforsch., A: Phys. Sci.* **1993**, *48*, 68. f) J. C. Ramírez, C. Soriano, R. O. Esquivel, R. P. Sagar, M. Hô, V. H. Smith, Jr., *Phys. Rev. A* **1997**, *56*, 4477.

32 P. E. M. Siegbahn, *J. Biol. Inorg. Chem.* **2006**, *11*, 695.

33 a) K. Wolinski, P. Pulay, *Chem. Phys. Lett.* **1987**, *140*, 225. b) K. Wolinski, P. Pulay, *J. Chem. Phys.* **1989**, *90*, 3647. c) B. O. Roos, P. Linse, P. E. M. Siegbahn, M. R. A. Blomberg, *Chem. Phys.* **1982**, *66*, 197. d) K. Andersson, P.-A. Malmqvist, B. O.

Roos, *J. Chem. Phys.* **1992**, *96*, 1218. e) K. Yamaguchi, *Int. J. Quantum Chem.* **1980**, *S14*, 269.

34 H. Tatewaki, S. Huzinaga, *J. Chem. Phys.* **1980**, *72*, 399.

35 P. J. Hay, *J. Chem. Phys.* **1977**, *66*, 4377.

36 P. C. Hariharan, J. A. Pople, *Theor. Chim. Acta* **1973**, *28*, 213.

37 W. J. Hehre, R. Ditchfild, J. A. Pople, *J. Chem. Phys.* **1972**, *56*, 2257.

38 We also carried out full geometry optimization on **1** using larger basis sets (6-31+G(d)) for the binding dioxygen (O5 and O6) and bridging oxygen (O_μ). However, the higher basis set afforded only a tiny difference (0.004 Å) in the distance between O5 and O6. In addition, it took several hundred steps of the electronic calculation to complete the geometry optimizations for these models. We did not use larger basis sets due to the considerable computational expense.

39 M. J. Frisch, G. W. Trucks, H. B. Schlegel, G. E. Scuseria, M. A. Robb, J. R. Cheeseman, J. A. Montgomery, Jr., T. Vreven, K. N. Kudin, J. C. Burant, J. M. Millam, S. S. Iyengar, J. Tomasi, V. Barone, B. Mennucci, M. Cossi, G. Scalmani, N. Rega, G. A. Petersson, H. Nakatsuji, M. Hada, M. Ehara, K. Toyota, R. Fukuda, J. Hasegawa, M. Ishida, T. Nakajima, Y. Honda, O. Kitao, H. Nakai, M. Klene, X. Li, J. E. Knox, H. P. Hratchian, J. B. Cross, V. Bakken, C. Adamo, J. Jaramillo, R. Gomperts, R. E. Stratmann, O. Yazyev, A. J. Austin, R. Cammi, C. Pomelli, J. W. Ochterski, P. Y. Ayala, K. Morokuma, G. A. Voth, P. Salvador, J. J. Dannenberg, V. G. Zakrzewski, S. Dapprich, A. D. Daniels, M. C. Strain, O. Farkas, D. K. Malick, A. D. Rabuck, K. Raghavachari, J. B. Foresman, J. V. Ortiz, Q. Cui, A. G. Baboul, S. Clifford, J. Cioslowski, B. B. Stefanov, G. Liu, A. Liashenko, P. Piskorz, I. Komaromi, R. L. Martin, D. J. Fox, T. Keith, M. A. Al-Laham, C. Y. Peng, A. Nanayakkara, M. Challacombe, P. M. W. Gill, B. Johnson, W. Chen, M. W. Wong, C. Gonzalez, J. A. Pople, *Gaussian 03, Revision C.02*, Gaussian, Inc., Wallingford CT, **2004**.

40 K. Zhang, E. A. Stern, F. Ellis, J. Sanders-Loehr, A. K. Shiemke, *Biochemistry* **1988**, *27*, 7470.

41 O. Hübner, K. Fink, W. Klopper, *Phys. Chem. Chem. Phys.* **2007**, *9*, 1911.

42 S. M. Gorun, S. J. Lippard, *Inorg. Chem.* **1991**, *30*, 1625.

43 T. Soda, Y. Kitagawa, T. Onishi, Y. Takano, Y. Shigeta, H. Nagao, Y. Yoshioka, K. Yamaguchi, *Chem. Phys. Lett.* **2000**, *319*, 223.

44 a) J. B. Howard, D. C. Rees, *Adv. Protein Chem.* **1991**, *42*, 199. b) L. Que, Jr., A. E. True, in *Progress in Inorganic Chemistry: Bioinorganic Chemistry*, ed. by S. J. Lippard, John Wiley & Sons, Inc., New York, **1990**, Vol. 38, p. 97.

45 a) K. Yamaguchi, F. Jensen, A. Dorigo, K. N. Houk, *Chem. Phys. Lett.* **1988**, *149*, 537. b) K. Yamaguchi, Y. Takahara, T. Fueno, K. N. Houk, *Theor. Chim. Acta* **1988**, *73*, 337.

46 a) Y. Takahara, K. Yamaguchi, T. Fueno, *Chem. Phys. Lett.* **1989**, *157*, 211. b) Y. Takahara, K. Yamaguchi, T. Fueno, *Chem. Phys. Lett.* **1989**, *158*, 95.

47 P. E. M. Siegbahn, M. R. A. Blomberg, *Chem. Rev.* **2000**, *100*, 421.

48 P. E. M. Siegbahn, M. R. A. Blomberg, *Annu. Rev. Phys. Chem.* **1999**, *50*, 221.

49 Y. Yoshioka, S. Kubo, K. Yamaguchi, I. Saito, *Chem. Phys. Lett.* **1998**, *294*, 459.